Proceedings of the Pakistan Academy of Sciences: A Physical and Computational Sciences 63(2): 99-113 (2026)

ISSN (Print): 2518-4245; ISSN (Online): 2518-4253
http://doi.org/10.53560/PPASA(63-2)713

Pakistan Academy of Sciences

Research Article

Integrated in Silico Analyses Reveal Diterpenoids from *Erythrophleum fordii* as Potential Inhibitors of Anti-Apoptotic Targets in Ovarian Cancer

Hung Duc Nguyen*

Faculty of Biology, Thai Nguyen University of Education, Thai Nguyen, Vietnam

Abstract: Ovarian cancer remains a major clinical challenge, particularly in advanced-stage disease, where relapse and resistance to platinum-taxane chemotherapy continue to limit therapeutic efficacy. Because anti-apoptotic Bcl-2 family proteins contribute to chemoresistance, myeloid cell leukemia 1 (Mcl-1) represents a relevant molecular target. This study evaluated five cassane-type diterpenoids from *Erythrophleum fordii* (CPD1-CPD5), previously reported to inhibit A2780 ovarian cancer cell growth, against Mcl-1 (PDB: 6UD2) using molecular docking, molecular dynamics simulation, Molecular Mechanics Generalised Born Surface Area (MM/GBSA), and Density Functional Theory (DFT) analysis, with paclitaxel as a reference. Docking placed all compounds within the BH3-binding groove and identified CPD2 (erythrophlesin F) as the top-ranked diterpenoid, with a docking score of -9.63 kcal/mol and favorable interactions with Asn223, Arg263, and Thr266. Molecular dynamics analysis indicated stable pocket occupancy for CPD2 and paclitaxel, while hydrogen-bond monitoring suggested greater persistence of polar contacts for CPD2. MM/GBSA supported favorable binding for both ligands, although paclitaxel displayed a more favorable mean binding free energy under the applied protocol. DFT descriptors further differentiated both compounds, with CPD2 showing a larger HOMO-LUMO gap and lower electrophilicity. These findings support CPD2 as a promising Mcl-1-binding candidate that warrants experimental validation.

Keywords: Apoptosis, DFT, Diterpenoid, *Erythrophleum fordii*, Mcl-1, Molecular Modeling.

1. INTRODUCTION

Ovarian cancer remains among the most fatal malignancies of the female reproductive tract. Survival outcomes are especially poor in advanced disease, where the five-year survival rate often does not exceed 30%. Much of this clinical burden arises from delayed diagnosis. In nearly 70-80% of cases, detection occurs only after substantial progression has already taken place. Recurrence further aggravates prognosis, with relapse reported in approximately 70-90% of patients even after first-line treatment [1]. Standard therapy for epithelial ovarian cancer relies on cytoreductive surgery followed by platinum-taxane chemotherapy [2]. Even so, long-term disease control is frequently undermined by tumor recurrence and the emergence of acquired drug resistance. Reduced sensitivity to paclitaxel-based treatment, for example, has been associated with adaptive cellular changes that weaken apoptotic signaling during mitotic stress and thereby permit continued tumor cell survival under sustained therapeutic exposure [3].

Resistance to therapy is closely linked to failure of apoptotic activation. The Bcl-2 protein family occupies a central position in this process by regulating mitochondrial outer membrane permeabilization and the downstream caspase cascade, both of which are essential for intrinsic apoptosis. Anti-apoptotic members of this family sequester BH3-only pro-apoptotic factors, suppress BAX/BAK activation, and in doing so elevate the threshold required for mitochondria-dependent cell death [4, 5]. Among these regulators, myeloid cell leukemia 1 (Mcl-1) has emerged as a particularly important determinant of cancer cell survival [6]. Elevated Mcl-1 activity has been implicated

Received: March 2026; Revised: May 2026; Accepted: June 2026
* Corresponding Author: Hung Duc Nguyen <hungnd@tnue.edu.vn>

in the suppression of multiple death-promoting signals and in the maintenance of drug-tolerant phenotypes across a range of malignancies, including chemotherapy-resistant tumors. As a result, Mcl-1 inhibition has gained recognition as a promising strategy for restoring antitumor sensitivity, a view reinforced by continued advances in the development and clinical assessment of BH3-mimetic compounds [7].

Natural products continue to occupy a central role in anticancer drug discovery because of their chemical diversity and long-standing pharmacological relevance. More than 60% of approved anticancer agents originate directly or indirectly from natural sources [8]. Major groups such as alkaloids, terpenoids, polyphenols, and quinones arise from biosynthetic pathways refined through evolution, often yielding molecular architectures well suited for interaction with biological macromolecules [9]. Compared with many fully synthetic collections, such compounds frequently offer greater structural complexity and broader target-recognition potential. Diterpenoids are particularly noteworthy within this landscape. This class has repeatedly been reported to possess marked antitumor activity, often accompanied by relatively low toxicity, and includes compounds capable of exerting both cytotoxic and chemosensitizing effects in diverse experimental models. Interest in diterpenoids has also increased because of documented influences on signaling pathways and drug-transport mechanisms associated with multidrug resistance [10, 11].

Species of the genus *Erythrophleum* are recognized sources of cassane-type diterpenoids. Several constituents isolated from *Erythrophleum fordii* have shown promising anticancer activity in ovarian cancer models, including inhibition of A2780 cell proliferation [12]. These observations raise the possibility that *E. fordii* diterpenoids may contain chemotypes able to interact with proteins governing apoptosis. That possibility remains insufficiently explored at the molecular level. In particular, protein-pocket recognition and ligand-specific binding determinants have not yet been defined in detail through systematic structure-based computational analysis.

Recent progress in structure-guided in silico methods has provided an efficient framework for compound prioritization, especially in natural-product research. Molecular docking, molecular dynamics (MD) simulation, and end-point binding free-energy estimation such as MM/GBSA now form a widely used workflow for evaluating ligand-protein interactions. Docking offers an initial view of binding geometry, whereas MD simulation captures the temporal behavior of complexes under solvated conditions that better approximate physiological environments [13]. Existing structural data on Mcl-1 enables precise assessment of ligand accommodation within its binding site. This assessment involves confirmation of docking configurations through redocking procedures and examination of ligand-protein interaction durability in aqueous settings. Concurrently, density functional theory (DFT) yields perspectives on ligand electronic attributes. Through evaluation of frontier molecular orbitals alongside additional DFT-derived metrics, comparisons of reactivity features that affect binding dynamics become feasible [14].

This investigation employed a unified computational methodology to analyze five diterpenoids extracted from *Erythrophleum fordii* (CPD1-CPD5), previously demonstrated to inhibit A2780 cell growth, as prospective binders to the anti-apoptotic protein Mcl-1. The crystallographic model 6UD2 served as the protein representation, with paclitaxel incorporated as a benchmark for contrasting binding patterns in the identical site. Molecular dynamics computations occurred in GROMACS via the CHARMM36 force field, while free energy estimations for binding utilized gmx_MMPBSA. DFT analyses in ORCA determined energies of frontier orbitals and associated theoretical descriptors. This approach appraised the diterpenoids' capacity to interact with the Mcl-1 site and sustain complex integrity, integrating docking alignments, simulation-derived energy evaluations, and quantum mechanical property descriptions into one cohesive protocol.

2. MATERIALS AND METHODS

2.1. Data Collection

The list of diterpenoids possessing anti-cancer activity against the A2780 ovarian cancer cell line was collected in the previous study [12]. Because A2780 is an established ovarian cancer cell model,

these compounds were selected to maintain a disease-relevant link between the previously reported cytotoxic activity and the present Mcl-1-targeted computational analysis. For detail, the selected ligands, including erythrophlesin E (CPD1), erythrophlesin F (CPD2), erythrophlesin C (CPD3), erythrophlesin G (CPD4) and 6α-hydroxydinorerythrophlamide (CPD5), have molecular formulas of $C_{46}H_{63}NO_{12}$, $C_{42}H_{61}NO_{10}$, $C_{43}H_{63}NO_{10}$, $C_{44}H_{63}NO_{12}$, $C_{23}H_{35}NO_7$, respectively, with molecular weights of 797.4350, 739.4295, 753.4452, 797.4350, and 437.2414 g/mol. The Paclitaxel, possessing a molecular formula of $C_{47}H_{51}NO_{14}$ and a molecular weight of 853.3310 g/mol, was chosen as the positive control (Figure 1).

2.2. Molecular Docking Analysis

Three-dimensional structures of the selected ligands were prepared in PDB format with BIOVIA Discovery Studio Visualizer, including addition of polar hydrogen atoms, assignment of Gasteiger partial charges, and allowance for full torsional flexibility. The Mcl-1 receptor structure (PDB ID: 6UD2) was obtained from the RCSB Protein Data Bank [15]. Receptor preprocessing in BIOVIA Discovery Studio involved removing crystallographic water molecules to align with an AutoDock-based approach that does not explicitly represent interfacial waters. Molecular docking was performed in AutoDock Tools using a grid box of 60 points along the x, y, and z axes with a grid spacing of 0.375 Å, centered on the binding site at x = 7.033 Å, y = 8.581 Å, and z = 98.593 Å. The grid center coordinates were defined based on the position of the co-crystallized ligand in the PDB 6UD2 structure. Conformational sampling and pose optimization were conducted using the Lamarckian genetic algorithm to prioritize low-energy binding orientations with favorable intermolecular contacts. Following docking, the top-ranked pose by predicted binding strength was examined in Discovery Studio Client 2024 and compared with docking results for Paclitaxel on the same receptor to contextualize relative binding features.

2.3. Molecular Dynamics Simulations

Molecular dynamics simulations were performed for the optimal docked complex with the 6UD2 protein over 100 ns using GROMACS 2024.4 with the CHARMM36 force field [16]. The receptor structure was curated in Swiss-PdbViewer to restore missing atoms and residues before simulation setup [17]. Ligand parameters and topology files were generated with SwissParam [18]. The protein-ligand assemblies were immersed in a triclinic periodic cell containing SPC water molecules, and NaCl was introduced to a final concentration of 0.15 M in order to approximate physiological ionic conditions. Adoption of an explicit-solvent environment permitted dynamic reorganization of interfacial water molecules during the simulation. Prior to trajectory generation, each system underwent 50,000 steps of energy minimization to remove unfavorable contacts and achieve an electrostatically balanced state. Equilibration was subsequently carried out in two stages: a

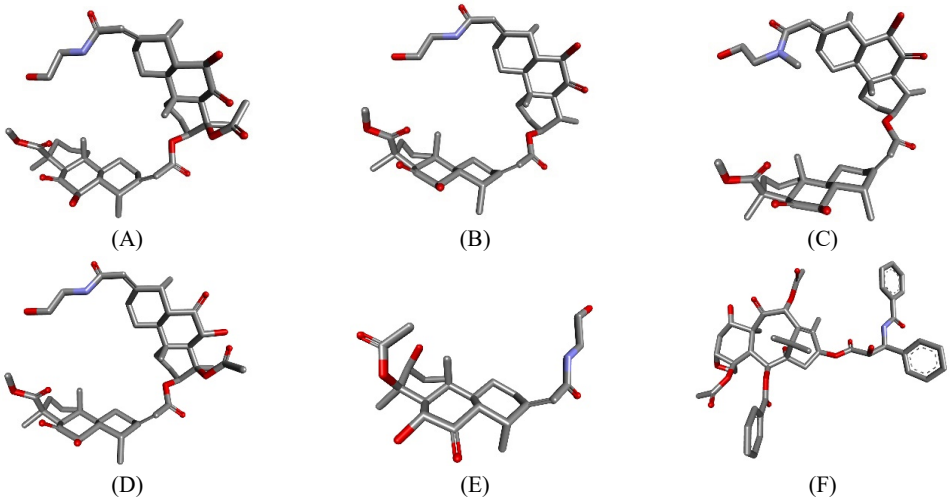

Fig. 1. 3D Structures of selected ligands. (A) CPD1, (B) CPD2, (C) CPD3, (D) CPD4, (E) CPD5, and (F) Paclitaxel.

200 ps NVT ensemble, followed by a 200 ps NPT ensemble, both maintained at 300 K and 1.0 bar. For each system, a single 100 ns production simulation was performed with a 2 fs integration step, and coordinates were saved at 10 ns intervals. Trajectory-derived parameters were analyzed in Grace, including root mean square deviation (RMSD), residue-wise root mean square fluctuation (RMSF), radius of gyration (Rg), number of hydrogen bonds (H-bonds), and solvent-accessible surface area (SASA). Conformational inspection and structural superposition were conducted in UCSF Chimera 1.13.3 to examine retention of the bound conformational state. Ligand poses extracted at 0 and 100 ns were overlaid within the binding site to evaluate the continuity of principal interaction patterns across the simulation period, with particular attention to hydrogen bonding, van der Waals contacts, and hydrophobic complementarity. Paclitaxel was used throughout as the reference ligand, with nomenclature retained consistently across all analyses.

2.4. Molecular Mechanics Generalised Born Surface Area (MM/GBSA) Analysis

Binding free energies for the CPD2-6UD2 and paclitaxel-6UD2 complexes were calculated with the gmx_MMPBSA protocol under the CHARMM36 force field [19]. Within this MM/GBSA framework, electrostatic solvation was represented by the generalized Born formalism under an implicit-solvent approximation, whereas the nonpolar contribution was obtained from solvent-accessible surface area-dependent terms. Energetic decomposition was performed from molecular dynamics trajectories using 125 evenly spaced snapshots collected every 80 ps across the 20-100 ns interval. Frame-averaged values were subsequently used to capture time-dependent variation in complex behavior and to compare relative binding favorability and stability under the applied simulation conditions [20].

2.5. Quantum Chemistry Computation Using the Density Functional Theory (DFT) Method

Geometry optimization of CPD2 and Paclitaxel was performed with the ORCA 6.1.0 quantum-chemistry suite. Starting conformations were built in Avogadro, and subsequent visualization together with molecular orbital inspection was carried out in IboView (v20211019) [21-24]. Density functional theory calculations were executed at the B3LYP/6-31G(d,p) level to obtain energetically minimized structures and an electronic-structure description suitable for reactivity assessment. This gas-phase B3LYP/6-31G(d,p) protocol was selected because it is commonly applied for geometry optimization and frontier molecular orbital analysis of natural-product-like compounds, enabling consistent comparison of electronic descriptors between CPD2 and paclitaxel. Based on the optimized geometries, frontier orbital energies (HOMO and LUMO) were obtained and used to derive the energy gap (ΔE) and related conceptual DFT descriptors, including chemical potential (μ), electronegativity (χ), global hardness (η), global softness (σ), and electrophilicity index (ω). These quantities were estimated under the Koopmans' theorem approximation to support the comparative interpretation of electronic characteristics and potential reactivity patterns of the investigated compounds [25, 26].

3. RESULTS AND DISCUSSION

3.1. Molecular Docking Analysis

Molecular docking constitutes a structure-guided approach for predicting ligand accommodation within a protein binding site and for prioritizing candidate complexes through scoring functions intended to approximate binding favorability [27]. Such scores, however, provide only a limited estimate because solvent effects, conformational adaptability of the receptor, and entropic contributions are represented in a simplified manner. For this reason, docking results are generally interpreted in conjunction with residue-level interaction patterns and, where possible, complemented by molecular dynamics simulation or binding free-energy refinement. In the present work, docking analysis was directed toward the anti-apoptotic protein Mcl-1 (PDB ID: 6UD2), a member of the BCL-2 family widely associated with apoptotic suppression and treatment resistance, and therefore regarded as a relevant target in contemporary anticancer research [28]. This target choice is relevant to ovarian cancer because impaired apoptotic signaling and resistance to platinum-taxane chemotherapy remain major barriers in ovarian cancer treatment, while the selected *E. fordii* diterpenoids were originally reported to inhibit A2780 ovarian cancer cell

growth [2, 3, 12]. The crystallographic entry 6UD2 provides an experimentally resolved Mcl-1 binding groove suitable for mapping ligand recognition features against a reference co-crystal environment. Before production docking, protocol validation is typically conducted by redocking the co-crystallized ligand and comparing the regenerated pose with the experimental conformation. This procedure yielded an RMSD of 0.5138 Å (Figure 2), indicating close reproduction of the pose. An RMSD cutoff of around 2 Å is widely used as a practical acceptance criterion for pose reproduction in benchmarking studies [29].

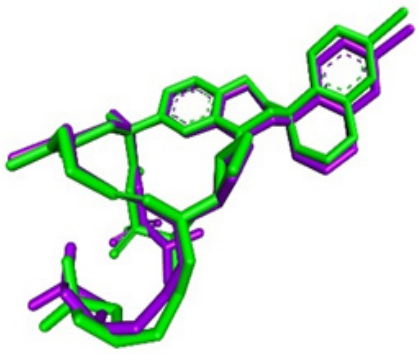

Fig. 2. Superimposition of the docked and native ligands for validation of the molecular docking protocol on protein 6UD2 (violet = native, green = docked).

After validation, candidate poses are ranked by docking energy and prioritized for interaction analysis within the Mcl-1 groove, focusing on non-covalent contacts such as hydrogen bonding, van der Waals complementarity, and hydrophobic packing, which collectively contribute to complex stabilization in BH3-like binding sites. Details of how the screened ligands interact with the 6UD2 binding cavity are summarized in Table 1, highlighting residues within the interaction zone and the dominant non-covalent interactions (hydrogen bonds, van der Waals, and hydrophobic interactions). Such interaction profiling is commonly used to rationalize docking poses and to prioritize candidates for downstream simulation or experimental evaluation.

Across the series, docking scores ranged from -7.39 to -9.63 kcal/mol, with CPD2 exhibiting the most favorable predicted affinity (-9.63 kcal/mol), followed by CPD3 (-9.28 kcal/mol) and CPD4 (-9.19 kcal/mol). CPD1 yielded a moderate affinity estimate (-8.80 kcal/mol), while CPD5 exhibited the poorest binding prediction among evaluated compounds (-8.17 kcal/mol). The comparator paclitaxel showed a less advantageous docking value (-7.39 kcal/mol) compared to chosen ligands,

Table 1. The interactions between the docked ligands and the protein 6UD2.

Docked ligands	Binding energy (kcal/mol)	Hydrogen bond interaction	Van der Waals interaction	Hydrophobic interaction
CPD1	-8.80	Gly262, Arg263, Leu267	Val220, Phe228, Leu235, Phe254, Asn260, Val265, Thr266, Gly271, Ile294	His224, Met231, Val249, Met250, Val253, Arg263, Phe270
CPD2	-9.63	Asn223, Arg263, Thr266	Val216, Val220, His224, Met231, Leu235, Phe254, Asn260, Val265, Gly271, Val274	Val249, Met250, Val253, Leu267, Phe270
CPD3	-9.28	His224, Val249, Arg263, Thr266	Val220, Asn223, Leu235, Leu246, Phe254, Val258, Asn260, Gly262, Val265, Gly271, Val274	Met231, Met250, Val253, Leu267, Phe270
CPD4	-9.19	His224, Arg263	Phe228, Met231, Leu235, Leu246, Val249, Met250, Thr266, Gly271, Val274, Leu290, Ile294	Ala227, Val253, Phe254, Leu267, Phe270
CPD5	-8.17	Arg263, Thr266	Val220, His224, Leu235, Leu246, Val249, Met250, Leu267, Val274	Met231, Val253, Phe254, Arg263, Phe270
Paclitaxel	-7.39	Arg263	Ala227, Phe228, Met231, Phe254, Gly262, Thr266, Phe270, Gly271, Leu290	His224, Leu246, Met250, Val253, Arg263, Leu267, Ile294

suggesting diminished anticipated stability in the identical site according to the employed metric. Docking evaluations usually involve relative assessments rather than definitive measures, where greater negativity correlates with enhanced conformational security based on observational scoring principles [30].

CPD2 achieved the strongest docking score and maintained active-site engagement with His224, Met231, Val249, Met250, Val253, Arg263, Leu267, and Phe270. Hydrogen-bonding interactions were identified with Asn223, Arg263, and Thr266, establishing a set of directional polar contacts across the entrance and central segment of the binding groove. Van der Waals complementarity extended beyond these residues to include Val216, Val220, His224, Met231, Leu235, Phe254, Asn260, Val265, Gly271, and Val274, indicating broad steric accommodation within the cavity (Figure 3(A)) [31]. Nonpolar contacts were distributed mainly around Val249, Met250, Val253, Leu267, and Phe270, a pattern consistent with stabilization through burial of hydrophobic surface area in the ligand-bound state. Taken together, the coexistence of defined polar anchoring at Asn223, Arg263 and Thr266 and compact hydrophobic packing across the Val249-Phe270 region provides a plausible structural basis for the superior docking score observed for this ligand relative to the remaining compounds [32]. The binding region in 6UD2 corresponds to the canonical BH3-recognition groove of Mcl-1, which is formed by a predominantly hydrophobic cleft responsible for accommodating the nonpolar face of BH3 helices and BH3-mimetic ligands. In the predicted binding mode, CPD2 extends along this groove and engages an extended hydrophobic surface defined by Val249, Met250, Val253, Leu267, and Phe270, consistent with occupation of the subpockets that govern BH3 recognition. Polar interactions involving Asn223, Arg263, and Thr266 appear to further constrain ligand orientation and support positional registration within the groove [33].

CPD1, CPD3, CPD4, and CPD5 occupied a broadly similar region of the Mcl-1 binding groove, with recurring contacts involving His224, Met231, Val249, Met250, Val253, Arg263, Leu267, and Phe270. These compounds shared a mixed polar-hydrophobic interaction pattern, although their docking scores and contact geometries varied. CPD3 and CPD4 showed relatively favorable docking scores and broad contact coverage, whereas CPD1 and CPD5 displayed less favorable predicted binding, possibly reflecting less optimal cavity filling or weaker polar anchoring. These observations suggest that the diterpenoid series generally fits within the same recognition region, but with ligand-specific differences in contact balance and shape complementarity.

Paclitaxel, used as a control ligand, engaged an expanded active-site set (His224, Ala227, Phe228, Met231, Met250, Val253, Arg263, Leu267, Phe270, Leu290). Hydrogen bonding was assigned to Arg263, while van der Waals interactions involved Ala227, Phe228, Met231, Phe254, Gly262, Thr266, Phe270, Gly271, and Leu290. Hydrophobic contacts were attributed to His224, Leu246, Met250, Val253, Arg263, Leu267, and Ile294 (Figure 3(B)). Despite the established clinical role of paclitaxel as a microtubule-directed chemotherapeutic agent, the lower docking score observed in this binding site suggests less favorable predicted accommodation within the present structural model. This difference in score supports preferential consideration of the CPD series for subsequent analysis in the 6UD2 pocket [34].

From a physicochemical standpoint, the interaction profile follows established determinants of protein-ligand recognition. Hydrogen bonds contribute spatial directionality and may constrain ligand orientation when donor-acceptor geometry is favorable, as reflected by contacts involving Asn223, Thr266, His224, and Arg263. By contrast, van der Waals interactions primarily reflect steric complementarity across the contour of the cavity. The hydrophobic cluster formed around Val249, Met250, Val253, Leu267, and Phe270 is likewise consistent with stabilization driven by nonpolar surface burial and interfacial water reorganization, particularly within grooves enriched in aliphatic and aromatic side chains. In combination, these non-covalent contributions provide a reasonable structural explanation for the docking hierarchy obtained in the present analysis [35, 36].

When docking score and interaction breadth are considered together, CPD2 emerges as the most compelling candidate for subsequent molecular dynamics evaluation. This prioritization is supported by the most favorable predicted binding

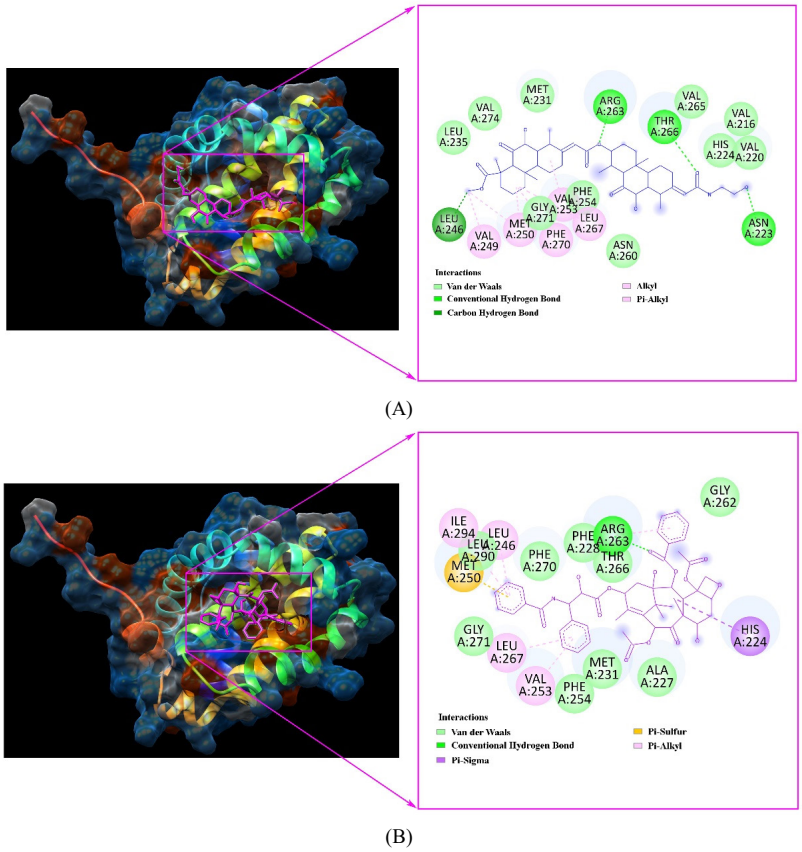

Fig. 3. Molecular docking model and 2D interaction diagram of CPD2 (A) and Paclitaxel (B) with 6UD2 protein.

energy (-9.63 kcal/mol), directional polar contacts with Asn223, Arg263, and Thr266, and extensive packing interactions spanning residues from Val216 to Val274, together with dense hydrophobic complementarity across the Val249-Phe270 region. CPD3 and CPD4 also exhibited favorable predicted recognition and broad residue engagement, indicating potential value as comparative systems in simulation studies or future structure-activity analysis. The 6UD2 structure represents human Mcl-1 in complex with an inhibitor, reinforcing the biological relevance of this pocket in apoptosis regulation and anticancer-target discovery.

3.2. Molecular Dynamics Simulations

Molecular dynamics (MD) simulations in drug design model the physical, time-dependent movements of atoms in biological systems to simulate interactions between drugs and targets. By accounting for molecular flexibility, MD enhances drug discovery by predicting binding affinities, optimizing lead compounds, identifying druggable sites, and revealing conformational changes, often refining results from docking studies [37]. In the present trajectories (100 ns), structural deviation, local flexibility, compactness, hydrogen-bond persistence, and solvent exposure were assessed for the CPD2-6UD2 and Paclitaxel-6UD2 complexes using root mean square deviation (RMSD), root mean square fluctuation (RMSF), radius of gyration (Rg), number of hydrogen bonds (H-bonds), and solvent-accessible surface area (SASA). Such descriptors are commonly used as complementary indicators of equilibration, residue-level mobility, global packing, and ligand-receptor interaction support in molecular dynamics-based screening approaches. The receptor model 6UD2 corresponds to an anti-apoptotic Mcl-1 co-crystal structure, aligning the simulations with an established apoptosis-evasion target relevant to therapeutic resistance in cancer biology. Accordingly, descriptors such as RMSD, RMSF, Rg, H-bonds, and SASA are routinely interpreted as complementary indicators of equilibration, local mobility, global compactness, and interaction continuity in protein-ligand systems. Consequently, the total energy and potential energy values for the

CPD2-6UD2 complex were found to be -362,971 kJ/mol and -449,240 kJ/mol, respectively. For the Paclitaxel-6UD2 complex, the total and potential energy values were -361,680 kJ/mol and -447,919 kJ/mol, respectively. The simulation system maintained equilibrium at 300 K.

The RMSD measures the average structural displacement relative to a reference conformation and is routinely used to assess trajectory convergence and global stability in biomolecular simulations. In the CPD2-6UD2 complex, RMSD values remained within 0.093-0.340 nm across 100 ns. The Paclitaxel-6UD2 complex showed a narrower distribution of 0.096-0.329 nm (Figure 4(A)). Both trajectories, therefore, occupied a low-RMSD regime (<0.35 nm), consistent with preserved overall fold during the simulation window. Transient excursions were visible but did not dominate the trajectories [37].

The RMSF was evaluated for Asp172-Gly326, covering the docking-defined recognition corridor and key residues such as His224, Ala227, Phe228, Met231, Val249-Val253, Arg263, Thr266, Leu267, Phe270, and Val274. In this region, both complexes show generally low fluctuations, with RMSF values mostly below 0.10 nm, consistent with a relatively stable local structure. Compared with Paclitaxel-6UD2, the CPD2-6UD2 complex displays slightly higher mobility across several subregions, particularly around Gly192-Met199, Arg201, and parts of the 230-250 segment, including the vicinity of Met231 and Val249-Val253 (Figure 4(B)). By contrast, residues forming the main recognition corridor remain comparatively restrained in both systems. The strongest increase in flexibility is confined to the C-terminal end, especially Glu322-Gly326, where both profiles rise sharply. Overall, the RMSF pattern indicates a stable binding region in both complexes, with Paclitaxel associated with marginally lower residue-level motion than CPD2.

The Rg reports mass-weighted spatial dispersion around the center of mass and is frequently interpreted as a compactness proxy during conformational sampling. Rg values for CPD2-6UD2 ranged from 1.455 to 1.543 nm. Paclitaxel-6UD2 ranged from 1.469-1.540 nm (Figure 4(C)). The overlapping Rg envelopes indicate comparable global compactness for both complexes, with no evidence of sustained expansion during 100 ns.

Hydrogen bonding contributes directionality and specificity in intermolecular recognition; in trajectories, hydrogen-bond counts are commonly monitored as a persistence descriptor rather than a sole affinity surrogate. In the CPD2-6UD2 system, the H-bond count fluctuated between 0 and 3, with frequent occupancy of 1-2 bonds and intermittent appearances of 3 bonds, particularly near the late portion of the trajectory. Digitized counts from the plot corresponded to proportions of approximately 33.7% (0 bonds), 33.2% (1 bond), 26.2% (2 bonds), and 6.9% (3 bonds) across the sampled frames. Paclitaxel-6UD2 fluctuated between 0 and 2 H-bonds; digitized proportions were approximately 81.2% (0 bonds), 14.3% (1 bond), and 4.5% (2 bonds) (Figure 4(D)). Based on these distributions, the estimated average H-bond number was approximately 1.06 bonds per frame for CPD2-6UD2, compared with 0.23 bonds per frame for paclitaxel-6UD2. This pattern supports higher hydrogen-bond persistence for CPD2 relative to Paclitaxel during the 100 ns window, consistent with docking assignments that placed Asn223/Arg263/Thr266 as principal polar anchors for CPD2 [15]. The higher average H-bond occupancy indicates more persistent polar stabilization of CPD2 within the Mcl-1 binding groove, thereby supporting its trajectory-level binding stability.

SASA tracks solvent exposure and can reflect breathing motions, ligand-induced burial, or changes in surface hydration; in practice, SASA complements RMSD and Rg by describing solvent-protein coupling. Over 100 ns, SASA values for CPD2-6UD2 spanned 88.30-101.03 nm^2. Paclitaxel-6UD2 spanned 91.70-98.69 nm^2 (Figure 4(E)). The CPD2 complex, therefore, showed a broader SASA dispersion, whereas Paclitaxel displayed a tighter envelope; however, both systems remained within a limited SASA band, consistent with the absence of major solvent-exposure transitions [38].

Across RMSD, RMSF (Asp172-Gly326), and Rg, both complexes preserved low-amplitude structural variability, indicating stable accommodation of each ligand in the crystallographic 6UD2 pocket. Hydrogen-bond monitoring differentiated the systems: CPD2 showed higher bond persistence and higher maximal occupancy (0-3) than Paclitaxel (0-2), aligning with docking-inferred polar contacts near Asn223, Arg263, and Thr266, and extensive hydrophobic packing around

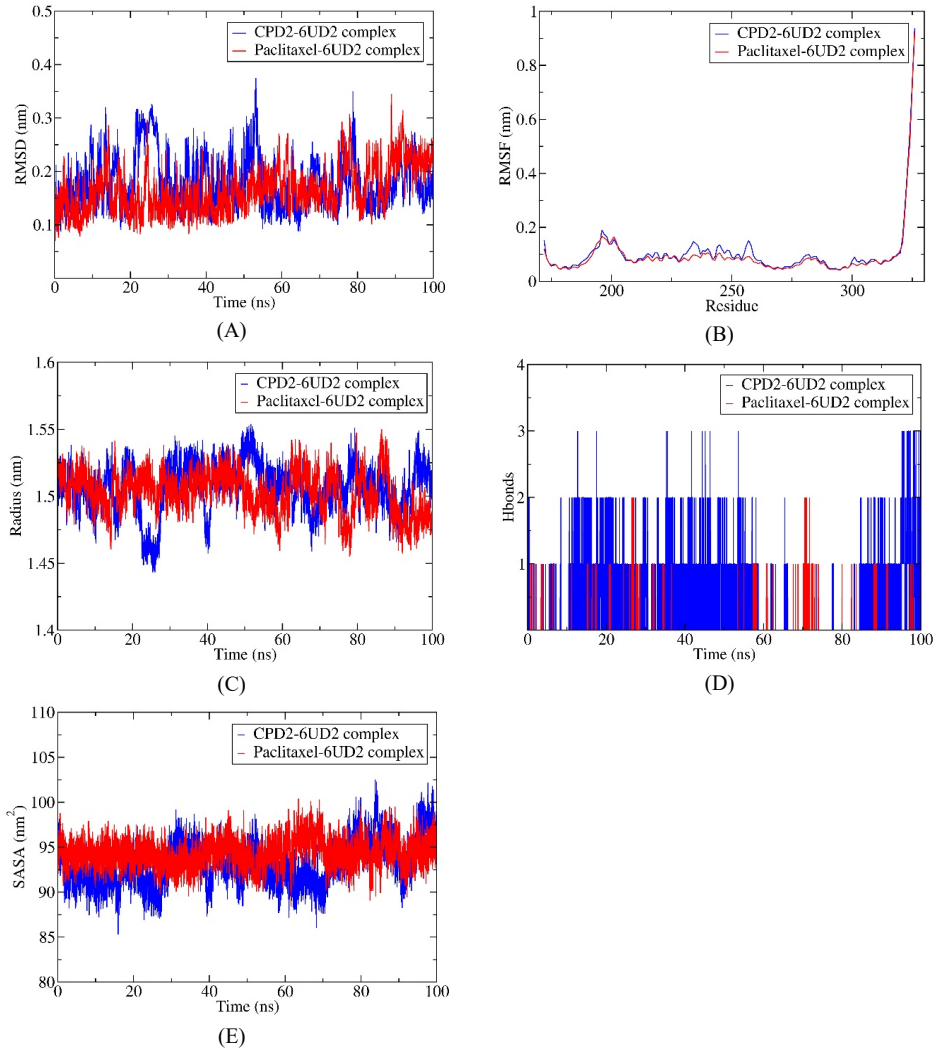

Fig. 4. Results of MD simulations for the bindings of CPD2 (blue) and Paclitaxel (red) with 6UD2 protein. (A) RMSD, (B) RMSF, (C) Rg, (D) Hbonds, and (E) SASA.

Val249, Met250, Val253, Leu267, and Phe270. SASA remained bound for both complexes, with CPD2 showing lower mean SASA but larger fluctuations than Paclitaxel, suggesting modest differences in solvent-exposure dynamics rather than large-scale conformational rearrangement.

3.3. Free Binding Energy (MM/GBSA) Analysis

Molecular Mechanics-Generalized Born Surface Area (MM/GBSA) has emerged as a crucial computational technique in modern drug discovery and natural product research, providing an efficient, accurate way to estimate binding free energies between macromolecules and small-molecule ligands. It bridges the gap between fast, less-accurate molecular docking scoring functions and slower, high-accuracy alchemical free energy methods [39]. Table 2 presents the MM/GBSA binding free-energy components (ΔVDWAALS, ΔEEL, ΔEGB, ΔESURF, ΔGGAS, ΔGSOLV) and the corresponding total binding free energy (ΔTOTAL) for the CPD2-6UD2 and Paclitaxel-6UD2 complexes, with mean values and standard deviations reported.

Both complexes show negative mean ΔTOTAL values, supporting a favorable association under the MM/GBSA decomposition used here. Paclitaxel-6UD2 yields ΔTOTAL = -35.77 ± 3.51 kcal/mol, whereas CPD2-6UD2 gives ΔTOTAL = -31.12 ± 4.00 kcal/mol. The mean difference is 4.65 kcal/mol in favor of Paclitaxel, indicating stronger predicted binding under the same computational protocol and sampling. A stronger gas-phase contribution primarily drives the more favorable

Table 2. Free energy of binding obtained using MM/GBSA calculations.

Energy Component	Average (kcal/mol)		Standard Deviation	
	CPD2-6UD2	Paclitaxel-6UD2	CPD2-6UD2	Paclitaxel-6UD2
ΔVDWAΔALS	-38.49	-50.29	4.17	3.71
ΔEEL	-10.55	-6.07	7.96	5.74
ΔEGB	22.72	27.42	7.46	6.20
ΔESURF	-4.79	-6.83	0.55	0.45
ΔGGAS	-49.05	-56.36	9.89	6.82
ΔGSOLV	17.93	20.59	7.08	6.10
ΔTOTAL	**-31.12**	**-35.77**	**4.00**	**3.51**

ΔTOTAL of Paclitaxel. ΔGGAS equals -56.36 ± 6.82 kcal/mol for Paclitaxel-6UD2 versus -49.05 ± 9.89 kcal/mol for CPD2-6UD2, a 7.31 kcal/mol advantage for Paclitaxel. Decomposition indicates that this advantage is dominated by dispersion/packing: ΔVDWAALS = -50.29 ± 3.71 kcal/mol (Paclitaxel) compared with -38.49 ± 4.17 kcal/mol (CPD2), i.e., 11.80 kcal/mol of van der Waals stabilization in favor of Paclitaxel. Such behavior is consistent with MM/GBSA practice, in which van der Waals terms often capture cavity complementarity and hydrophobic packing. Electrostatics partially compensates for the van der Waals difference. The Coulombic term ΔEEL is more favorable for CPD2-6UD2 (-10.55 ± 7.96 kcal/mol) than for Paclitaxel-6UD2 (-6.07 ± 5.74 kcal/mol), producing a 4.48 kcal/mol electrostatic advantage for CPD2. The net ΔGGAS ranking nevertheless remains Paclitaxel-favored because the magnitude of the van der Waals difference exceeds the opposing electrostatic shift [40].

Implicit-solvent contributions oppose binding for both ligands (positive ΔGSOLV), consistent with desolvation penalties in GBSA-type models. ΔGSOLV equals 20.59 ± 6.10 kcal/mol for Paclitaxel-6UD2 and 17.93 ± 7.08 kcal/mol for CPD2-6UD2, giving CPD2 a 2.66 kcal/mol lower solvation penalty. This difference arises mainly from the polar GB term: ΔEGB = 27.42 ± 6.20 kcal/mol (Paclitaxel) versus 22.72 ± 7.46 kcal/mol (CPD2), i.e., 4.70 kcal/mol lower polar desolvation for CPD2. The nonpolar surface term favored both complexes, with a modest advantage observed for paclitaxel. ΔESURF was calculated as -6.83 ± 0.45 kcal/mol for the paclitaxel-6UD2 complex and -4.79 ± 0.55 kcal/mol for CPD2-6UD2, corresponding to a 2.04 kcal/mol difference in favor of paclitaxel for the nonpolar solvation component. The solvation profile therefore reflected a differentiated energetic balance: CPD2 showed a lower penalty from the polar contribution, whereas paclitaxel displayed more favorable nonpolar surface energetics. The associated standard deviations indicated moderate variation across the sampled conformational ensemble, a pattern commonly observed in end-point free-energy approaches. Variability for ΔTOTAL remained relatively restricted, with standard deviations of 4.00 kcal/mol for CPD2-6UD2 and 3.51 kcal/mol for paclitaxel-6UD2. Greater fluctuation was evident for ΔGGAS (9.89 and 6.82 kcal/mol, respectively) and for the polar solvation term ΔEGB (7.46 and 6.20 kcal/mol, respectively), in agreement with the recognized sensitivity of MM/GBSA energy components to conformational microstates and dielectric representation.

Within the present MM/GBSA framework, the paclitaxel-6UD2 complex yielded the more favorable average binding free-energy estimate (-35.77 ± 3.51 kcal/mol) relative to CPD2-6UD2 (-31.12 ± 4.00 kcal/mol). This difference was driven primarily by a stronger van der Waals contribution for paclitaxel (-50.29 versus -38.49 kcal/mol), although part of that advantage was counterbalanced by more favorable electrostatic interaction energy and a lower polar solvation penalty in the CPD2 complex (ΔEEL, -10.55 versus -6.07 kcal/mol; ΔEGB, 22.72 versus 27.42 kcal/mol). Such a component distribution is consistent with the general behavior of MM/GBSA analyses, in which packing-related terms frequently dominate ΔGGAS, whereas implicit-solvent contributions influence the final rank ordering. Accordingly, interpretation remains most reliable in a comparative

sense within a uniform computational protocol. Although paclitaxel showed a more favorable MM/GBSA value, CPD2 was still prioritized because its selection was based on the integrated docking-MD-DFT assessment rather than MM/GBSA alone. In particular, CPD2 exhibited the best docking score among the diterpenoids, stable binding-site occupancy during MD simulation, and more persistent hydrogen-bond interactions, supporting its relevance as the lead *E. fordii* diterpenoid scaffold for further investigation.

3.4. Quantum Chemistry Computation Using the DFT Method

Density functional theory (DFT) represents an efficient and powerful computational tool for analyzing the electronic properties of isolated molecules and drug delivery systems, offering superior accuracy compared to molecular mechanics (MM) for studying reaction mechanisms, binding interactions, and enzyme inhibition [41]. Within conceptual DFT frameworks, the highest occupied molecular orbital (EHOMO) is linked to electron donation tendencies, while the lowest unoccupied molecular orbital (ELUMO) relates to electron acceptance. The HOMO-LUMO gap (ΔE) is commonly associated with electronic reactivity, where a smaller gap suggests increased polarizability and more favorable charge redistribution. Table 3 presents DFT-derived quantum descriptors for CPD2 and paclitaxel, including frontier orbital energies (EHOMO and ELUMO), the HOMO-LUMO gap (ΔE), and global reactivity indices (μ, χ, η, σ, and ω).

CPD2 exhibited an EHOMO of -9.6064 eV, while paclitaxel showed -8.6942 eV, indicating a higher electron donation propensity for paclitaxel. Regarding electron acceptance, CPD2 presented ELUMO = 3.3664 eV, and paclitaxel exhibited ELUMO = 2.1568 eV, with paclitaxel's lower LUMO suggesting a more accessible acceptor orbital [42]. The HOMO-LUMO gap for CPD2 was larger (ΔE = 12.9728 eV) compared to paclitaxel (ΔE = 10.8510 eV), reflecting a more rigid electronic structure for CPD2 and greater electronic flexibility for paclitaxel (Figure 5) [43].

The chemical potential (μ) for CPD2 was -3.1200 eV, while for paclitaxel, it was -3.2687 eV, implying a stronger thermodynamic tendency for electron stabilization in paclitaxel. Electronegativity (χ), treated as the negative of μ, also reflected this trend, with paclitaxel exhibiting a higher value (3.2687 eV vs. 3.1200 eV for CPD2) [44]. Chemical hardness (η) was 6.4864 eV for CPD2 and 5.4255 eV for paclitaxel, indicating that CPD2 is electronically stiffer, while paclitaxel is more electronically adaptable. The inverse parameter, softness (σ), was 0.1542 eV^{-1} for CPD2 and 0.1843 eV^{-1} for paclitaxel, with paclitaxel showing higher softness, suggesting more flexibility in response to external perturbation. The electrophilicity index (ω) was higher for paclitaxel (0.9846 eV) compared to CPD2 (0.7504 eV), indicating a stronger electrophilic character for paclitaxel under this conceptual framework [45]. These results highlight CPD2's more stable electronic profile, marked by a deeper HOMO, a higher LUMO, and a larger ΔE, compared to paclitaxel, which is characterized by a smaller ΔE, a higher HOMO energy, and greater electronic responsiveness.

Taken together, the integrated computational approach positions CPD2 as a promising Mcl-1-binding scaffold, offering stable binding and consistent interaction persistence. Although paclitaxel showed a more favorable MM/GBSA binding free energy, CPD2 remains the lead diterpenoid candidate because it exhibited the strongest docking score among the screened compounds, stable binding-site occupancy during MD simulation, and greater hydrogen-bond

Table 3. Quantum descriptors of CPD2 and Paclitaxel.

Molecule	EHOMO (eV)	ELUMO (eV)	ΔE (eV)	μ (eV)	χ (eV)	η (eV)	σ (eV^{-1})	ω (eV)
CPD2	-9.6064	3.3664	12.9728	-3.1200	3.1200	6.4864	0.1542	0.7504
Paclitaxel	-8.6942	2.1568	10.8510	-3.2687	3.2687	5.4255	0.1843	0.9846

EHOMO (eV): highest occupied molecular orbitals; ELUMO (eV): lowest unoccupied molecular orbitals; ΔE (eV): energy gap; μ (eV): chemical potential; χ (eV): electronegativity; η (eV): hardness; σ (eV^{-1}): softness; ω (eV): electrophilicity index.

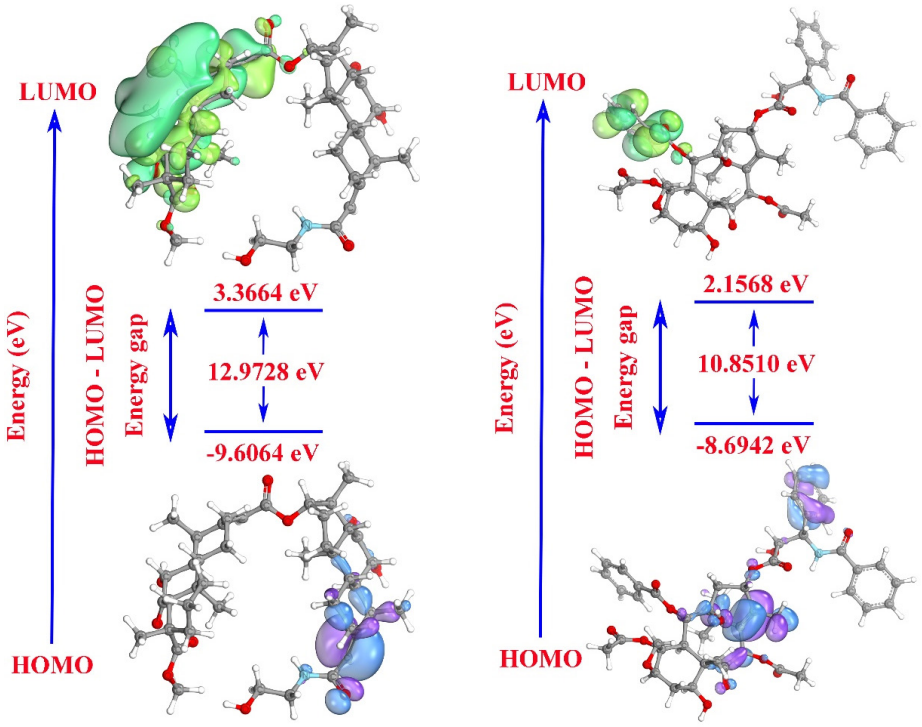

Fig. 5. HOMO and LUMO surface diagrams of CPD2 (A) and Paclitaxel (B).

persistence within the Mcl-1 groove. In the context of ovarian cancer, these findings suggest that CPD2 may provide a useful starting scaffold for exploring apoptosis-related therapeutic strategies, particularly because the compounds were selected from *E. fordii* with reported activity against A2780 ovarian cancer cells. However, experimental validation is necessary to confirm Mcl-1 inhibition and establish biological relevance in ovarian cancer models. The lack of in vitro and in vivo validation remains a significant limitation, and future work should focus on biochemical binding assays, apoptosis assays in ovarian cancer cell lines, and early-stage ADMET profiling. Additionally, further optimization of the structure to enhance packing interactions while maintaining polar anchoring, along with an assessment of off-target interactions within the BCL-2 family, would be crucial for evaluating the potential therapeutic development of CPD2.

4. CONCLUSIONS

This investigation presents a comprehensive computational analysis of diterpenoids derived from *E. fordii* as potential inhibitors of Mcl-1 (PDB ID: 6UD2), a protein associated with apoptosis resistance in ovarian cancer. Molecular docking simulations indicated favorable accommodation of the diterpenoid series within the canonical binding groove of Mcl-1, with CPD2 emerging as the most promising candidate. CPD2 exhibited a more favorable docking score than paclitaxel (-9.63 kcal/mol vs. -7.39 kcal/mol) and demonstrated a balanced interaction profile, characterized by directional polar anchors (Asn223, Arg263, Thr266) and nonpolar packing (Val249, Met250, Val253, Leu267, Phe270). Molecular dynamics simulations over 100 ns supported the stability of CPD2's binding mode, with both complexes remaining in low-deviation regimes (mean RMSD 0.192 ± 0.053 nm for CPD2-6UD2 and 0.172 ± 0.038 nm for paclitaxel-6UD2), showing similar compactness (Rg of 1.51 nm). CPD2 maintained a more persistent hydrogen-bond network compared to paclitaxel, which further supports its strong interaction stability. MM/GBSA analysis confirmed the energetic favorability of both compounds, with paclitaxel displaying stronger van der Waals stabilization (-50.29 kcal/mol vs. -38.49 kcal/mol), while CPD2 showed stronger electrostatic contributions and reduced polar solvation penalties. DFT calculations highlighted paclitaxel's greater electronic adaptability (smaller ΔE and higher ω), whereas CPD2 exhibited a more rigid electronic

structure (larger ΔE and lower ω), indicating distinct electronic profiles for each compound.

5. ETHICAL STATEMENT

Ethical approval is not required, as this work does not include any studies involving human or animal subjects.

6. CONFLICT OF INTEREST

The author declares that there is no conflict of interest.

7. FUNDING

No funding was received to conduct this research.

8. AUTHORSHIP CONTRIBUTION

Hung Duc Nguyen: the sole responsibility for the conception of the study, presented results, and manuscript preparation. All data were generated in-house and that no paper mill was used. All results were interpreted solely by the author; Grammarly and Google Translate were used for English language refinement.

9. REFERENCES

1. M. Arcieri, V. Tius, S. Filippin, G. Aletti, D. Lorusso, A. Fagotti, J. Sehouli, I. Zapardiel, P. De Iaco, P. Scollo, and *et al*. Management of patients with epithelial ovarian cancer: A systematic comparison of international guidelines from scientific societies (AIOM-BGCS-ESGO-ESMO-JGSO-NCCN-NICE). *Cancers* 17(24): 3915 (2025). https://doi.org/10.3390/cancers17243915
2. M. Nunes, C. Bartosch, M.H. Abreu, A. Richardson, R. Almeida, and S. Ricardo. Deciphering the molecular mechanisms behind drug resistance in ovarian cancer to unlock efficient treatment options. *Cells* 13(9): 786 (2024). https://doi.org/10.3390/cells13090786
3. R. Goel, P. Upadhyay, R. Garg, D. Gulwani, and T.D. Singh. Overcoming paclitaxel resistance in ovarian cancer cells using DN200434, an inverse agonist of estrogen-related receptor gamma (ERRγ). *Biochemical and Biophysical Research Communications* 778: 152351 (2025). https://doi.org/10.1016/j.bbrc.2025.152351
4. J. Kale, E.J. Osterlund, and D.W. Andrews. BCL-2 family proteins: Changing partners in the dance towards death. *Cell Death & Differentiation* 25(1): 65-80 (2018). https://doi.org/10.1038/cdd.2017.186
5. I. Jaya, F. Safriadi, I. Wijaya, P. Pitaloka, E. Afifah, F.S. Medina, and M.H. Bashari. Role of Bcl-2 family anti-apoptosis inhibition in overcoming therapeutic resistance in prostate cancer: A systematic review. *Critical Reviews in Oncology/Hematology* 215: 104895 (2025). https://doi.org/10.1016/j.critrevonc.2025.104895
6. M. Mohiuddin. Targeting MCL-1 to overcome therapeutic resistance and improve cancer mortality. *Health Science Reports* 8(10): e71390 (2025). https://doi.org/10.1002/hsr2.71390
7. W. Xiang, C.Y. Yang, and L. Bai. MCL-1 inhibition in cancer treatment. *OncoTargets and therapy* 11: 7301-7314 (2018). https://doi.org/10.2147/OTT.S146228
8. S.T. Asma, U. Acaroz, K. Imre, A. Morar, S.R. Shah, S.Z. Hussain, D. Arslan-Acaroz, H. Demirbas, Z. Hajrulai-Musliu, F.R. Istanbullugil, A. Soleimanzadeh, D. Morozov, K. Zhu, V. Herman, A. Ayad, C. Athanassiou, and S. Ince. Natural products/bioactive compounds as a source of anticancer drugs. *Cancers* 14(24): 6203 (2022). https://doi.org/10.3390/cancers14246203
9. A. Naeem, P. Hu, M. Yang, J. Zhang, Y. Liu, W. Zhu, and Q. Zheng. Natural Products as Anticancer Agents: Current Status and Future Perspectives. *Molecules* 27(23): 8367 (2022). https://doi.org/10.3390/molecules27238367
10. Z. Deng, I. Bakunina, H. Yu, J. Han, A. Dömling, M.J.U. Ferreira, and J. Zhang. Research progress on natural diterpenoids in reversing multidrug resistance. *Frontiers in Pharmacology* 13: 815603 (2022). https://doi.org/10.3389/fphar.2022.815603
11. A. Sharmila, P. Bhadra, C. Kishore, C.I. Selvaraj, J. Kavalakatt, and A. Bishayee. Nanoformulated Terpenoids in cancer: A review of therapeutic applications, mechanisms, and challenges. *Cancers* 17(18): 3013 (2025). https://doi.org/10.3390/cancers17183013
12. D. Du, J. Qu, J.M. Wang, S.S. Yu, X.G. Chen, S. Xu, S.G. Ma, Y. Li, G.Z. Ding, and L. Fang. Cytotoxic cassaine diterpenoid-diterpenoid amide dimers and diterpenoid amides from the leaves of *Erythrophleum fordii*. *Phytochemistry* 71(14): 1749-1755 (2010). https://doi.org/10.1016/j.phytochem.2010.07.004
13. A. Vidal-Limon, J.E. Aguilar-Toalá, and A.M. Liceaga, Integration of molecular docking analysis and molecular dynamics simulations for studying food proteins and bioactive peptides. *Journal of Agricultural and Food Chemistry* 70(4): 934-943 (2022). https://doi.org/10.1021/acs.jafc.1c06110
14. S. Liu. The evolving quest for chemical understanding

in the quantum age. *Journal of Chemical Theory and Computation* 21(20): 10068-10079 (2025). https://doi.org/10.1021/acs.jctc.5c01299

15. G. Rescourio, A.Z. Gonzalez, S. Jabri, B. Belmontes, G. Moody, D. Whittington, X. Huang, S. Caenepeel, M. Cardozo, A.C. Cheng, D. Chow, and *et al*. Discovery and in vivo evaluation of macrocyclic Mcl-1 inhibitors featuring an α-hydroxy phenylacetic acid pharmacophore or bioisostere. *Journal of Medicinal Chemistry* 62(22): 10258-10271 (2019). https://doi.org/10.1021/acs.jmedchem.9b01310
16. D.V.D. Spoel, E. Lindahl, B. Hess, G. Groenhof, A.E. Mark, and H.J.C. Berendsen. GROMACS: Fast, flexible, and free. *Journal of Computational Chemistry* 26(16): 1701-1718 (2005). https://doi.org/10.1002/jcc.20291
17. N. Guex and M.C. Peitsch. SWISS-MODEL and the Swiss-Pdb Viewer: An environment for comparative protein modeling. *Electrophoresis* 18(15): 2714-2723 (1997). https://doi.org/10.1002/elps.1150181505
18. V. Zoete, M.A. Cuendet, A. Grosdidier, and O. Michielin. SwissParam: A fast force field generation tool for small organic molecules. *Journal of Computational Chemistry* 32(11): 2359-2368 (2011). https://doi.org/10.1002/jcc.21816
19. M.S. Valdés-Tresanco, M.E. Valdés-Tresanco, P.A. Valiente, and E. Moreno. gmx_MMPBSA: A new tool to perform end-state free energy calculations with GROMACS. *Journal of Chemical Theory and Computation* 17(10): 6281-6291 (2021). https://doi.org/10.1021/acs.jctc.1c00645
20. H.D. Nguyen. Unveiling the anti-apoptotic mechanism of magnolialide as a colorectal cancer inhibitor via molecular modeling, ADMET, and MMGBSA analysis. *Physical Chemistry Research* 13(4): 783-796 (2025). https://doi.org/10.22036/pcr.2025.535946.2708
21. F. Neese. Software update: The ORCA program system-version 6.0. *WIREs Computational Molecular Science* 15(2): e70019 (2025). https://doi.org/10.1002/wcms.70019
22. G. Knizia and J.E. Klein. Electron flow in reaction mechanisms-revealed from first principles. *Angewandte Chemie International Edition* 54(18): 5518-5522 (2015). https://doi.org/10.1002/anie.201410637
23. G. Knizia. Intrinsic atomic orbitals: An unbiased bridge between quantum theory and chemical concepts. *Journal of Chemical Theory and Computation* 9(11): 4834-4843 (2013). https://doi.org/10.1021/ct400687b
24. M.D. Hanwell, D.E. Curtis, D.C. Lonie, T. Vandermeersch, E. Zurek, and G.R. Hutchison. Avogadro: an advanced semantic chemical editor, visualization, and analysis platform. *Journal of Cheminformatics* 4(1): 17 (2012). https://doi.org/10.1186/1758-2946-4-17
25. J. Luo, Z.Q. Xue, W.M. Liu, J.L. Wu, and Z.Q. Yang. Koopmans' Theorem for Large Molecular Systems within Density Functional Theory. *The Journal of Physical Chemistry A* 110(43): 12005-12009 (2006). https://doi.org/10.1021/jp063669m
26. R. Das, J.L. Vigneresse, and P.K. Chattaraj. Chemical reactivity through structure-stability landscape. *International Journal of Quantum Chemistry* 114(21): 1421-1429 (2014). https://doi.org/10.1002/qua.24706
27. Z. Ma, A. Ajibade, and X. Zou. Docking strategies for predicting protein-ligand interactions and their application to structure-based drug design. *Communications in Information and Systems* 24(3): 199 (2024). https://doi.org/10.4310/cis.241021221101
28. S.I. Tantawy, N. Timofeeva, A. Sarkar, and V. Gandhi. Targeting MCL-1 protein to treat cancer: opportunities and challenges. *Frontiers in Oncology* 13: 1226289 (2023). https://doi.org/10.3389/fonc.2023.1226289
29. D.A. Schaller, C.D. Christ, J.D. Chodera, and A. Volkamer. Benchmarking Cross-Docking Strategies in Kinase Drug Discovery. *Journal of Chemical Information and Modeling* 64(23): 8848-8858 (2024). https://doi.org/10.1021/acs.jcim.4c00905
30. A.O.H. Zayed. Optimizing protein-ligand docking through machine learning: algorithm selection with AutoDock Vina. *Discover Chemistry* 2(1): 164 (2025). https://doi.org/10.1007/s44371-025-00246-4
31. Q. Sun. The hydrophobic effects: Our current understanding. *Molecules* 27(20): 7009 (2022). https://doi.org/10.3390/molecules27207009
32. T.V. Szalai, D. Bajusz, R. Börzsei, B.Z. Zsidó, J. Ilaš, G.G. Ferenczy, C. Hetényi, and G.M. Keserű. Effect of water networks on ligand binding: Computational predictions vs experiments. *Journal of Chemical Information and Modeling* 64(23): 8980-8998 (2024). https://doi.org/10.1021/acs.jcim.4c01291
33. A. McGriff and W.J. Placzek. Phylogenetic analysis of the MCL1 BH3 binding groove and rBH3 sequence motifs in the p53 and INK4 protein families. *PLoS One* 18(1): e0277726 (2023). https://doi.org/10.1371/journal.pone.0277726

34. J. Sharifi-Rad, C. Quispe, J.K. Patra, Y.D. Singh, M.K. Panda, G. Das, C.O. Adetunji, O.S. Michael, O. Sytar, L. Polito, J. Živković, N. Cruz-Martins, M. Klimek-Szczykutowicz, H. Ekiert, M.I. Choudhary, S.A. Ayatollahi, B. Tynybekov, F. Kobarfard, A.C. Muntean, I. Grozea, S.D. Dastan, M. Butnariu, A. Szopa, and D. Calina. Paclitaxel: Application in modern oncology and nanomedicine-based cancer therapy. *Oxidative Medicine and Cellular Longevity* 2021(1): 3687700 (2021). https://doi.org/10.1155/2021/3687700
35. G.G. Ferenczy and M. Kellermayer. Contribution of hydrophobic interactions to protein mechanical stability. *Computational and Structural Biotechnology Journal* 20: 1946-1956 (2022). https://doi.org/10.1016/j.csbj.2022.04.025
36. V.A. Adhav and K. Saikrishnan. The realm of unconventional noncovalent interactions in proteins: Their significance in structure and function. *ACS Omega* 8(25): 22268-22284 (2023). https://doi.org/10.1021/acsomega.3c00205
37. O.M.H. Salo-Ahen, I. Alanko, R. Bhadane, A.M.J.J. Bonvin, R.V. Honorato, S. Hossain, A.H. Juffer, A. Kabedev, M. Lahtela-Kakkonen, A.S. Larsen, E. Lescrinier, P. Marimuthu, M.U. Mirza, G. Mustafa, A. Nunes-Alves, T. Pantsar, A. Saadabadi, K. Singaravelu, and M. Vanmeert. Molecular dynamics simulations in drug discovery and pharmaceutical development. *Processes* 9(1): 71 (2021). https://doi.org/10.3390/pr9010071
38. R.F. de Freitas and M. Schapira. A systematic analysis of atomic protein-ligand interactions in the PDB. *MedChemComm* 8(10): 1970-1981 (2017). https://doi.org/10.1039/C7MD00381A
39. E. Wang, H. Sun, J. Wang, Z. Wang, H. Liu, J.Z.H. Zhang, and T. Hou. End-point binding free energy calculation with MM/PBSA and MM/GBSA: Strategies and applications in drug design. *Chemical Reviews* 119(16): 9478-9508 (2019). https://doi.org/10.1021/acs.chemrev.9b00055
40. L. Dong, P. Li, and B. Wang. Enhancing MM/P(G)BSA methods: Integration of formulaic entropy for improved binding free energy calculations. *Journal of Computational Chemistry* 46(10): e70093 (2025). https://doi.org/10.1002/jcc.70093
41. I. Ahmad, V. Jagatap, and H. Patel. Application of density functional theory (DFT) and response surface methodology (RSM) in drug discovery. In: Phytochemistry, computational tools and databases in drug discovery. C. Egbuna, M. Rudrapal, and H. Tijjani (Eds.). *Elsevier, Amsterdam, Netherlands* pp. 371-392 (2023). https://doi.org/10.1016/B978-0-323-90593-0.00004-6
42. V. Hadigheh Rezvan, Molecular structure. HOMO-LUMO, and NLO studies of some quinoxaline 1,4-dioxide derivatives: Computational (HF and DFT) analysis. *Results in Chemistry* 7: 101437 (2024). https://doi.org/10.1016/j.rechem.2024.101437
43. Y. Xu, Q. Chu, D. Chen, and A. Fuentes. HOMO-LUMO Gaps and Molecular Structures of Polycyclic Aromatic Hydrocarbons in Soot Formation. *Frontiers in Mechanical Engineering* 7: 744001 (2021). https://doi.org/10.3389/fmech.2021.744001
44. P. Geerlings. From density functional theory to conceptual density functional theory and biosystems. *Pharmaceuticals* 15(9): 1112 (2022). https://doi.org/10.3390/ph15091112
45. R. Pal and P.K. Chattaraj. Electrophilicity index revisited. *Journal of Computational Chemistry* 44(3): 278-297 (2023). https://doi.org/10.1002/jcc.26886